Charged particle tracking without magnetic field: optimal measurement of track momentum by a Bayesian analysis of the multiple measurements of deflections due to multiple scattering

Mikael Frosini[a], Denis Bernard[a]

[a] *LLR, Ecole Polytechnique, CNRS/IN2P3, 91128 Palaiseau, France*

Abstract

We revisit the precision of the measurement of track parameters (position, angle) with optimal methods in the presence of detector resolution, multiple scattering and zero magnetic field. We then obtain an optimal estimator of the track momentum by a Bayesian analysis of the filtering innovations of a series of Kalman filters applied to the track.

This work could pave the way to the development of autonomous high-performance gas time-projection chambers (TPC) or silicon wafer γ-ray space telescopes and be a powerful guide in the optimisation of the design of the multi-kilo-ton liquid argon TPCs that are under development for neutrino studies.

Key words: track momentum measurement, multiple scattering, Kalman filter, Bayesian approach, noise covariance estimation, algebraic Riccati equation, magnetic-field free, time projection chamber, neutrino detector, gamma-ray telescope

1. Introduction

1.1. γ-ray astronomy

A huge effort is in progress to design γ-ray telescopes able to bridge the sensitivity gap that extends between the upper end of the high-sensitivity energy range of past and present X-ray telescopes and the lower end of the high-

Email addresses: denis.bernard at in2p3.fr (Denis Bernard)

sensitivity energy range of the Fermi-LAT telescope, that is, approximately $0.1 - 100\,\mathrm{MeV}$.

On the low-energy side of the gap, tracking of the electron issued from the first Compton scattering of an incident photon enables a major improvement of the precision of the reconstruction of the direction of the incident photon ([1] and references therein) that induces an impressive improvement of the true-photon-background rejection and therefore of the point-like-source sensitivity. A serious limitation of that ETCC (electron tracking Compton camera) scheme arises though, as the effective area undergoes a sharp drop for photon energies above $0.5\,\mathrm{MeV}$, due to the fact that the recoil electron can exit on the side and escape energy measurement [1]: electron momentum measurement inside the time projection chamber (TPC) itself is highly desirable.

On the high-energy side of the gap, novel approaches improve the sensitivity by improving the single-photon angular resolution by using converters having a lower-Z than that of the tungsten plates of the EGRET / Fermi-LAT series. Using a series of silicon wafer active targets placed at a distance of each other, at the same time the material in which the photon converts and in which the tracks are tracked, enables an improvement of $\approx$ a factor of three in the angular resolution at $100\,\mathrm{MeV}$ with respect to the LAT [2–9] at the cost of a lower average active target density. Similar values of the angular resolution are achieved using a high-spatial-resolution, homogeneous, high-density material such as an emulsion [10].

If the trend to lower densities is pushed to the use of a gaseous detector, the angular resolution with respect to the LAT can increase up to a factor of ten at $100\,\mathrm{MeV}$ [11] and the single-track angular resolution is so good that the azimuthal angle of the e^+e^- pair can be measured with a good enough precision to enable the measurement of the linear polarization fraction of the incident radiation [12–14]. Gas detectors enable the detection of low-energy photons close to the pair-creation threshold where most of the statistics lie for cosmic sources (Fig. 1 of [15]), something which is critical for polarimetry.

Astrophysicists also need to measure the energy of incoming photons and

therefore the momentum of the conversion electron(s). This can be achieved using a number of techniques.

- In a calorimeter, the total energy of the photon is absorbed and measured.
- In a magnetic spectrometer, the trajectory of a particle with electric charge q and momentum p in a magnetic field B is curved with a curvature radius $\rho = p/(qB)$: from a measurement of ρ, one obtains a measurement of p and in the end of the photon energy E.
- In a transition radiation detector (TRD), the energy of the radiation emitted in the forward direction by a charged particle at the interface between two media that have different refraction indices is proportional to the Lorentz factor γ of the particle, enabling a direct measurement. The low number of emitted photons per track per interface has lead to the development of multi-foil systems that suffer destructive interference at high energies. Appropriate configurations have showed saturation values larger than $\gamma \approx 10^4$, which implies that a measurement can be done up to a photon energy of $\approx 10\,\mathrm{GeV}$ [16].

The low-density active targets that have been considered above can provide a large effective area telescope only with a large volume ($\mathcal{O}(\mathrm{m}^3)$) and therefore the mass of the additional device used for energy measurement is a serious issue onboard a space mission. **In this document we first address the performance of the track momentum measurement from measurements of the angular deflections of charged tracks due to multiple scattering during the propagation in the tracker itself**.

1.2. Large noble-liquid TPCs for neutrino physics

Neutrino oscillation is a well established phenomenon and several experiments are being prepared with the goals:

- To test the occurrence of CP violation in the neutral lepton sector, i.e. to measure the only free complex phase δ of the Pontecorvo-Maki-Nakagawa-

Sakata (PMNS) matrix with enough precision to determine its non-compatibility with zero,

- To determine unambiguously the 3 neutrino mass ordering, i.e. to solve the sign ambiguity of the square mass difference Δm^2_{31}.

Not only the (vacuum propagation) phase term that involves δ changes sign upon $\nu \leftrightarrow \overline{\nu}$ exchange, but the term that describes the interaction with matter changes sign too as our Earth contains much more electrons than positrons. "In the few-GeV energy range, the asymmetry from the matter effect increases with baseline as the neutrinos pass through more matter, therefore an experiment with a longer baseline [is] more sensitive to the neutrino mass hierarchy. For baselines longer than ≈ 1200 km, the degeneracy between the asymmetries from matter and CP-violation effects can be resolved" [17]. Large distances imply low fluxes, that is, huge detectors and, to match the $\sin(\Delta mL/4E_\nu)$ oscillation function, high-energy neutrinos. So we should be prepared to measure the momentum of high-momentum muons in huge non-magnetised detectors such as liquid argon (lAr) TPCs.

The DUNE experiment expects to be able to measure muon momenta with a relative precision of $\approx 18\%$ [18], based on a past ICARUS work [19]. They "anticipate that the resolution will deteriorate for higher-energy muons because they scatter less", though. Given the $\mathrm{d}E/\mathrm{d}x$ of 0.2 GeV/m of minimum ionising particles in lAr, a typical 6 GeV/c muon produces a long track: it should be interesting to study to what extent an optimal analysis of the thousands of measurements per track, at their ≈ 3 mm sampling pitch, can do better.

1.3. Track momentum measurement from multiple scattering

The measurement of track momentum using multiple scattering was pioneered by Molière [20] and has been used since, in particular in the context of emulsion detectors (recent accounts can be found in [21, 22]).

In a practical detector consisting of N detection layers, the precision of the deflection measurement and therefore of the momentum measurement is

affected by the precision, σ, of the measurement of the position of the track when crossing each layer: the combined square deflection angle summed up over the whole track length therefore includes contributions from both the scattering angle and the detector precision. Bernard has optimized the longitudinal "cell" length over which each deflection angle is measured [11] and obtains a value of the relative momentum precision σ_p/p that scales as $p^{1/3}$, but the fact that the track position precision can improve when the cell length is extended and several measurements are combined was not taken into account in [11]. **In the present document we study an optimal method of momentum measurement with a tracker that has a finite (non zero) precision.**

In Section 2 we revisit optimal tracking methods in a context where the momentum of the particle is known. This allows us to present concepts and notations that are used later in the paper. We also extend the results published in the past by the use of more powerful methods.

The optimal precision of track measurements obtained in Sec. 2 can be obtained by performing the fit with a Kalman filter (KF), a tool that was imported in our field by Frühwirth [23]. In section 3 we give a brief summary of Kalman filter tracking in a Bayesian formalism. In magnetic spectrometers, the particle momentum takes part both in the particle state vector through the curvature of the trajectory and in the magnitude of multiple scattering. The precision of the magnetic measurement is most often so good that the momentum can rightfully be considered as being perfectly known in the expression of the multiple scattering. In our case of a zero magnetic field, it is not the case. A Kalman filter is the optimal estimate for linear system models with additive white noise, such is the case for multiple scattering (process noise) and detector precision (measurement noise), but at the condition that the optimal Kalman gain be used in the expression, that is, that the track momentum be known. In section 4, we use the Bayesian method developed by Matisko and Havlena [24] to obtain an optimal estimator of the process noise covariance, and therefore of the track momentum

[1]. We implement this method and characterize its performance on Monte Carlo (MC) simulated tracks. We check that the momentum measurement is unbiased within uncertainties. We obtain a heuristic analytical expression of the relative momentum uncertainty.

Numerical examples are given for a homogeneous gas detector such as an argon TPC and for a silicon-wafer detector:

- TPC gas, argon, 5 bar, $\sigma = l = 0.1\,\mathrm{cm}$, $L = 30\,\mathrm{cm}$ [12];
- Silicon detector $N = 56$, $\Delta x = 500\,\mu\mathrm{m}$-thick wafers spaced by $l = 1\,\mathrm{cm}$, with a single point precision of $\sigma = 70\,\mu\mathrm{m}$ [8].

In this work a number of approximations are done: only the Gaussian core of the multiple-scattering angle distribution is considered and the non-Gaussian tails due to large-angle single scatters are neglected. The small logarithmic correction term in the expression of the RMS multiple scattering angle, θ_0, is neglected

$$\theta_0 \approx \frac{p_0}{\beta p}\sqrt{\frac{\Delta x}{X_0}}, \tag{1}$$

where $p_0 = 13.6\,\mathrm{MeV}/c$ is the "multiple-scattering constant", Δx is the matter thickness through which the particle propagates and X_0 is its radiation length (Eqs. (33.14), (33.15), (33.17) of [26]). In the case of a homogeneous detector, the thickness of the scatterer is equal to the length of the longitudinal sampling, $l = \Delta x$. We assume relativistic particles ($\beta \approx 1$) without loss of generality. Only the first-order term (angle deflection) of multiple scattering is taken into account which is legitimate for the thin detectors considered here; the 2nd-order transverse displacement (eq. (33.19) of [26]) is neglected. Continuous ($\mathrm{d}E/\mathrm{d}x$) and discrete (BremsStrahlung radiation) energy losses are also neglected. In TPCs in which the signal is sampled, most often the electronics applies a shaping

[1] Attempts of estimation of track momenta based on the use of a Kalman filter have been performed in the past, with little success. The un-validated un-characterized study of Ref. [25], for example, shows a poor relative resolution of $\sigma_p/p = 30 - 40\%$ and that does not vary with the true particle momentum between $50\,\mathrm{MeV}/c$ and $2\,\mathrm{GeV}/c$, which is a bad symptom.

of the pulse before digitisation, that creates a short scale longitudinal correlation between successive measurements that we neglect too. Also the limitations of pattern recognition, that is, in the case of γ-ray telescopes, of the assignment of each hit to one of two close tracks, are not addressed.

Note that in the two main parts of this work (section 2 and sections 3-4) we have made our best to follow the notations of Refs. [27, 28] and of [24], respectively, and that they turn out to differ to some extent.

2. Tracking

An optimal tracking makes use of the full $N \times N$ covariance matrix of the N measurements, including multiple scattering (correlation terms). This is most often impractical in modern trackers that provide a huge number of measurements for each track. The first successful attempt to perform a recursive determination of the covariance matrix was achieved by Billoir [27]. He considered the paraxial propagation of a charged track along the x axis inside a magnetic field oriented along z: close to the particle origin, the trajectory is a straight line in the (x, z) plane, and a parabola osculatrix to the true circle in the (x, y) plane. As we examine here the case of a magnetic-field-free tracker, the propagation (in the (x, z) and in the (x, y) planes) is approximated by straight lines (already using Innes notations [28] but assuming $B = 0$):

$$y = a + b \times x. \tag{2}$$

Astronomers obviously have a special interest in the slope b, that is, in the paraxial direction of the track at the conversion vertex.

The (a, b) correlation matrix is named V and the information matrix, $I \equiv V^{-1}$. Billoir develops a recursive method in which the fit propagates along the track, adding the information gain (measurement) and loss (scattering) at each layer. He obtains the information matrix at layer $n + 1$ from the information matrix at layer n [27, 28]:

$$I_{n+1} = D^T \left(I_n^{-1} + B \right)^{-1} D + M, \tag{3}$$

where D is the drift matrix that propagates the track from layer n to layer $n+1$,

$$D = \begin{bmatrix} 1 & l \\ 0 & 1 \end{bmatrix}, \tag{4}$$

l is the layer spacing. B is the scattering matrix,

$$B = \begin{bmatrix} 0 & 0 \\ 0 & sl \end{bmatrix}, \tag{5}$$

where $s \equiv \left(\frac{p_0}{p}\right)^2 \frac{\Delta x}{lX_0}$ is the average multiple-scattering angle variance per unit track length, $\theta_0^2 = s \times l$. M is the measurement matrix,

$$M = \begin{bmatrix} \imath l & 0 \\ 0 & 0 \end{bmatrix}, \tag{6}$$

where $\imath \equiv \frac{N+5}{L\sigma^2} \approx \frac{1}{l\sigma^2}$ is the information density per unit track length, $L = N \times l$ is the full detector thickness.

Billoir considers the two particular cases of "scatters at one point" (detector layers separated by an empty space) that we name here a segmented detector and "uniformly distributed scattering" (homogeneous detector) [27]. These concepts are defined more precisely below, following Innes [28].

2.1. Segmented detector

Expressing I_n as $I_n = A_n B_n^{-1}$ ([29], page 149) we obtain

$$\begin{bmatrix} A_{n+1} \\ B_{n+1} \end{bmatrix} = \begin{bmatrix} D^T + MD^{-1}B & MD^{-1} \\ D^{-1}B & D^{-1} \end{bmatrix} \begin{bmatrix} A_n \\ B_n \end{bmatrix}, \tag{7}$$

and

$$I_{n+1} = A_{n+1} B_{n+1}^{-1}. \tag{8}$$

Noting

$$\Phi \equiv \begin{bmatrix} D^T + MD^{-1}B & MD^{-1} \\ D^{-1}B & D^{-1} \end{bmatrix}, \tag{9}$$

we obtain

$$\begin{bmatrix} A_n \\ B_n \end{bmatrix} = \Phi^n \begin{bmatrix} A_0 \\ B_0 \end{bmatrix}. \tag{10}$$

A_n and B_n are obtained from the eigenvalues of Φ. The covariance matrix becomes $V_n = B_n A_n^{-1}$. We initialise the recurrence with $A_0 = I_0 = 0$, $B_0 = 1$. If $\begin{bmatrix} A_n \\ B_n \end{bmatrix}$ is a solution of eq. (8), then for any $\beta > 0$,

$$\frac{1}{\beta^n} \begin{bmatrix} A_n \\ B_n \end{bmatrix} = \frac{1}{\beta^n} \Phi^n \begin{bmatrix} A_0 \\ B_0 \end{bmatrix} \tag{11}$$

is a solution too. Noting $\tilde{A}_n = \dfrac{A_n}{\beta^n}$, $\tilde{B}_n = \dfrac{B_n}{\beta^n}$, $\tilde{\Phi} = \dfrac{\Phi}{\beta}$, we obtain

$$\begin{bmatrix} \tilde{A}_n \\ \tilde{B}_n \end{bmatrix} = \tilde{\Phi}^n \begin{bmatrix} \tilde{A}_0 \\ \tilde{B}_0 \end{bmatrix}, \tag{12}$$

with $V_n = \tilde{B}_n \tilde{A}_n^{-1}$. Φ is found to satisfy

$$\Phi^T J \Phi = J, \tag{13}$$

with

$$J = \begin{bmatrix} 0 & 0 & 1 & 0 \\ 0 & 0 & 0 & 1 \\ -1 & 0 & 0 & 0 \\ 0 & -1 & 0 & 0 \end{bmatrix}, \tag{14}$$

from which Φ is a symplectic matrix. General theorems enable a classification of Φ eigenvalues into two "invert" and "conjugate" blocks, respectively (eq. (10) of [30])

$$\left\{ \alpha, \alpha^*, \frac{1}{\alpha}, \frac{1}{\alpha^*} \right\}, \tag{15}$$

where "$*$" denotes complex conjugation. We choose α to have a norm larger than unity, $|\alpha| > 1$. We obtain [31]

$$\alpha(x) = \frac{1}{2} j x^2 + \frac{1}{2} \left(-x^4 + 4 j x^2 \right)^{\frac{1}{2}} + 1, \tag{16}$$

where j is the imaginary unit and $x \equiv \frac{l}{\lambda}$ is the detector longitudinal sampling normalized to the detector scattering length at momentum p [28]:

$$\lambda \equiv \frac{1}{\sqrt[4]{\imath s}}. \tag{17}$$

An exploration of the consequences of a variation of the initialisation of the recurrence parameters shows that the system converges to the same solution $\alpha(x)$ regardless of the values of A_0, B_0. $B_0 \neq 0$ is needed so that I_0 is defined. With $B_0 = 1$, $I_0 = A_0 = 0$ simply assumes that no *a priori* information is known about the track.

We study the convergence of the covariance matrix while the Billoir mechanism is in progress along the track (increasing n) by setting $\beta = |\alpha|$, that is, $\tilde{\Phi} = \frac{1}{|\alpha|}\Phi$. $\tilde{\Phi}$ has two eigenvalues with modulus unity and two eigenvalues with modulus $\frac{1}{|\alpha|^2}$. The unity-modulus eigenvalues could be a major nuisance in the behaviour of I_n as a function of n, but when applying the Billoir mechanism we observe that for some reason the amplitude the so-induced oscillating terms is zero. The convergence behaviour is then driven by the two other eigenvalues, that is, by terms proportional to $\frac{1}{|\alpha|^{2n}}$. That exponential convergence is illustrated in Fig. 1 that shows the value of the detector thickness normalized to the detector scattering length, u [28],

$$u \equiv \frac{L}{\lambda}, \tag{18}$$

for which $\frac{1}{|\alpha|^{2n}} < 10^{-4}$, as a function of x.

Note that the homogeneousness parameter x and the thickness parameter u have a similar dependence on track momentum p, as $u = x \times N$.

2.1.1. Segmented detector: Thick detector limit

The asymptotic expression at high n, that is, at high u (thick detector) is reached after the Billoir mechanism (eq. (3)) has converged: we obtain the discrete Riccati equation:

$$I = D^T \left(I^{-1} + B\right)^{-1} D + M. \tag{19}$$

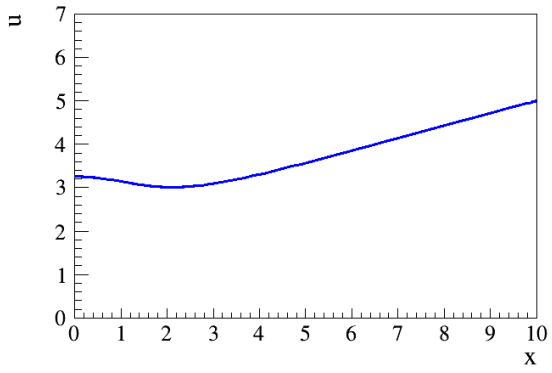

Figure 1: Value of u for which $\frac{1}{|\alpha|^{2n}} < 10^{-4}$ as a function of x (from eq. (16)). For $x < 5$, convergence is reached for a detector thickness of 4λ.

When the geometric, the multiple scattering and the measurement properties of the detector are uniform (at least piecewise) the dynamics of the particle is described by a time-invariant system and eq. (19) is referred to as the "algebraic" Riccati equation (DARE). Equation (19) has four solutions, but the fact that the asymptotically stable solution must be positive definite (Theorem 2.2 of [30]) leaves us with only one.

Segmented detector: Exact solution.

We obtain [31]

$$V = \begin{pmatrix} \frac{4l^3 s}{x^3\left(2x+\sqrt{x^2+4j}-\sqrt{x^2-4j}\right)} & \frac{sl^2\left(\sqrt{x^2+4j}+\sqrt{x^2-4j}\right)}{x^2\left(\sqrt{-x^2-4j}-\sqrt{4j-x^2}-2jx\right)} \\ -\frac{4l^2 s}{x^2\left(\sqrt{-x^2-4j}-jx\right)\left(jx+\sqrt{4j-x^2}\right)} & \frac{2ls\left(\sqrt{x^2+4j}+\sqrt{x^2-4j}\right)}{\left(x+\sqrt{x^2+4j}\right)\left(jx+\sqrt{4j-x^2}\right)} \end{pmatrix}. \quad (20)$$

Even though it is not explicit from eq. (20), V is found to be a real matrix, which is decent for a covariance matrix.

Segmented thick detector: Small x behaviour: Homogeneous detector limit.

The Taylor expansion close to $x = 0$ is found to be

$$V_{aa} = \frac{\sqrt{2}}{\imath\lambda}\left[1 - \frac{x}{\sqrt{2}} + \frac{3}{8}x^2 - \frac{\sqrt{2}}{8}x^3 + \frac{9}{128}x^4 + O[x^5]\right], \quad (21)$$

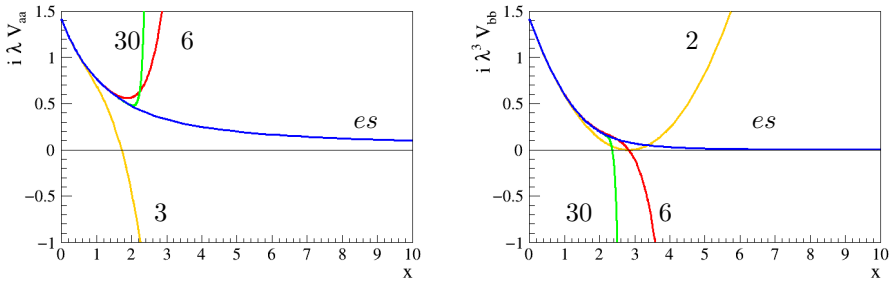

Figure 2: Thick detector: $\imath\lambda V_{aa}$ and $\imath\lambda^3 V_{bb}$ as a function of x. Comparison of the Taylor expansions to several orders, eqs. (21) and (22) to the exact solution "es", eq. (20).

$$V_{bb} = \frac{\sqrt{2}}{\imath\lambda^3}\left[1 - \frac{x}{\sqrt{2}} + \frac{1}{8}x^2 + \frac{x^3}{128} - \frac{1}{1024}x^4 + O[x^5]\right]. \tag{22}$$

These expressions are similar[2] to what was found by Billoir ([27], p364, no magnetic field) and Innes ([28], eq. (8), magnetic field). The Taylor expansion is found to converge for $x \lesssim 2$ (Fig. 2).

Segmented thick detector: Large x behaviour: Coarse segmentation limit.

The asymptotic behaviour of the coarsely instrumented detector (high x) is presented in Fig. 3.

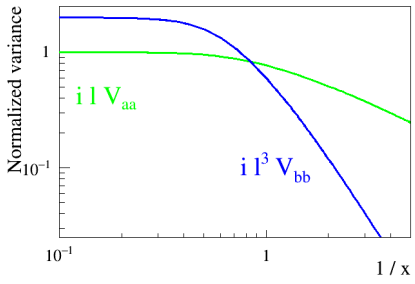

Figure 3: Thick detector: Normalized variance $\imath l V_{aa}$ and $\imath l^3 V_{bb}$ as a function of $1/x$ (eq. (20)).

[2] We have detected a misprint, though: the factor $-5/8$ in their expressions of V_{aa} is here corrected to $3/8$.

For $1/x = 0$ we obtain $\imath l V_{aa} = 1$ and $\imath l^3 V_{bb} = 2$, that is the obvious

$$V_{aa} = \sigma^2, \quad V_{bb} = 2\left(\frac{\sigma}{l}\right)^2 : \tag{23}$$

the scattering is so intense that the intercept (angle) measurement is based on the first (two first) layer(s), respectively. A thick coarse detector can be defined by $1/x < 0.5$, that is, $l > 2\lambda$ (Fig. 3). The $\frac{1}{x}$ Taylor expansion is:

$$V_{aa} = \frac{1}{\imath l}\left[1 - \frac{1}{x^4} + O\left(\frac{1}{x^8}\right)\right], \tag{24}$$

$$V_{bb} = \frac{1}{\imath l^3}\left[2 - \frac{10}{x^4} + O\left(\frac{1}{x^8}\right)\right]. \tag{25}$$

2.2. Homogeneous Detector

A homogeneous detector is described having l tend to 0 while s and $\imath$ are kept constants. Fig. 4 shows that for all values of u, the intercept and angle variances become very close to the homogeneous limit ($x = 0$) for $x \lesssim 0.2$.

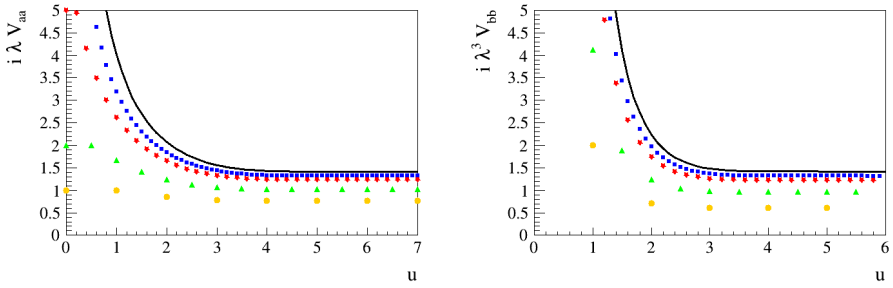

Figure 4: Normalized covariance coefficients $\imath\lambda V_{aa}$ (left) and $\imath\lambda^3 V_{bb}$ (right) as a function of u for various values of $x \in \{0, 0.1, 0.2, 0.5, 1\}$. Curve, $x = 0$ (eq. (37)); squares, $x = 0.1$; stars, $x = 0.2$; triangles, $x = 0.5$; bullets, $x = 1.0$. In both cases (a and b), $x \lesssim 0.2$ is found to be a good approximation of the homogeneous detector ($x = 0$).

From the discrete evolution equation, eq. (3), and denoting $I_n = I(nl) = I(L)$, we obtain

$$\dot{I}(L) = D'^T I(L) + I(L)D' - I(L)B'I(L) + M', \tag{26}$$

where the dot denotes the derivation with respect to L and with

$$D' = \begin{bmatrix} 0 & 1 \\ 0 & 0 \end{bmatrix}, \quad B' = \begin{bmatrix} 0 & 0 \\ 0 & s \end{bmatrix}, \quad M' = \begin{bmatrix} \imath & 0 \\ 0 & 0 \end{bmatrix}. \tag{27}$$

After convergence (thick detector), we obtain the continuous algebraic Riccati equation (CARE):

$$D'^T I(L) + I(L)D' - I(L)B'I(L) + M' = 0, \tag{28}$$

Homogeneous Detector: Small u behaviour.

We first use Innes' method to compute an approximate solution. Attempting a Taylor expansion in u, $I(u) = \sum I^k u^k$, we obtain:

$$\begin{aligned} I^0 &= 0, \\ I^1 &= M', \\ I^{k+1} &= \frac{1}{k+1}\left(-\sum_{i=0}^{k} I^i B' I^{k-i} + D'^T I^k + I^k D'\right). \end{aligned} \tag{29}$$

- In our case ($B = 0$, no curvature) we obtain:

$$V_{aa} = \frac{4}{\imath\lambda u}\left[1 + \frac{u^4}{416} - \frac{127u^8}{15\,891\,876\,000} + O(u^{12})\right] \tag{30}$$

$$V_{bb} = \frac{12}{\imath\lambda^3 u^3}\left[1 + \frac{13u^4}{420} - \frac{13\,429u^8}{529\,200} + O(u^{12})\right] \tag{31}$$

- For $B \neq 0$ and a fit with curvature, we obtain the results of Innes (eq. (9) of [28]).

These Taylor expansions converge for $u \lesssim 3.5$ (no curvature, Fig. 5) and $u \lesssim 7.0$ (with curvature, [28]). The thin detector ($u = 0$) value of V_{bb} for $B = 0$ is found to be smaller than that for $B \neq 0$ by a factor of 16, as was discussed in the corrigendum of [11]: in a fit with curvature, the correlation between the curvature and the angle at the end(s) of the track degrades the angular resolution badly; this lasts until $u \approx 1$ that is $L \approx \lambda$ (plot not shown), after which all is flooded by multiple scattering anyway.

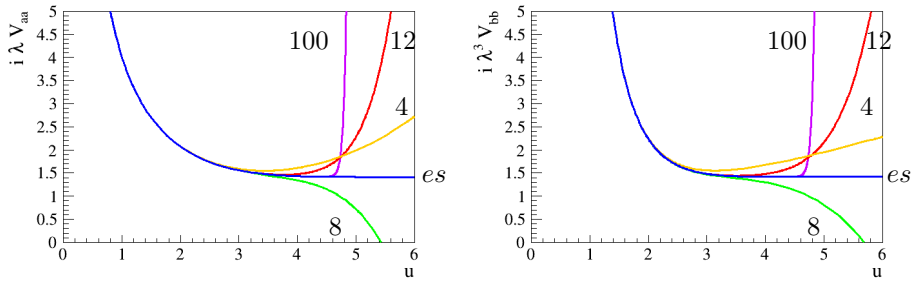

Figure 5: Homogeneous detector: $\imath\lambda V_{aa}$ and $\imath\lambda^3 V_{bb}$ as a function of u. Comparison of the Taylor expansions to several orders, eqs. (30) and (31), to the exact solution obtained from the resolution "es" of eqs. (33)-(34).

Homogeneous Detector: Large u behaviour: Thick detector limit.

Searching for expressions that are valid at high u, we follow again Innes and search a solution of the continuous equation for V that is similar to eq. (26) for I. Here the Taylor expansion is searched in $1/u$. Searching a solution parametrized as $V(u) = V_0 + \dfrac{1}{u}V_1$, we obtain

$$V_{aa} = \frac{\sqrt{2}}{\imath\lambda}, \qquad V_{bb} = \frac{\sqrt{2}}{\imath\lambda^3}. \tag{32}$$

These values agree with that of eqs. (21), (22) for $x = 0$. The term proportional to $1/u$ that was present in the case with curvature (eq. (11) of [28]) cancels here, which is related to the exponential convergence seen on eq. (37) (see also Fig. 7).

2.2.1. Homogeneous thick detector: Exact solution

We solve the continuous algebraic Riccati equation in a way similar to the discrete case [29]: Expressing

$$\Phi' = \begin{bmatrix} D' & M' \\ B' & -D'^T \end{bmatrix} \tag{33}$$

and $I(L) = X(L)Y^{-1}(L)$, and taking $I(0) = 0$, we obtain:

$$\begin{pmatrix} X(L) \\ Y(L) \end{pmatrix} = \exp\left[L\Phi'\right] \begin{pmatrix} 0 \\ 1 \end{pmatrix}. \tag{34}$$

Φ' satisfies

$$\Phi'^{T} J \Phi'^{-1} = -J \tag{35}$$

and is a hamiltonian matrix (section (4.8) of [29], [32]), which implies that $\exp[\Phi']$ is a symplectic matrix and therefore that $\Re\{\mathrm{Tr}(\Phi')\} = 0$. Furthermore all eigenvalues of Φ' are found to be non singular [31]:

$$\mathrm{Spec}(\Phi') = \left\{ \frac{1}{\lambda} e^{\frac{-3j\pi}{4}}, \frac{1}{\lambda} e^{\frac{-j\pi}{4}}, -\frac{1}{\lambda} e^{\frac{-3j\pi}{4}}, -\frac{1}{\lambda} e^{\frac{-j\pi}{4}} \right\}. \tag{36}$$

Solving eq. (34) we obtain [31]

$$V = \begin{pmatrix} \frac{\sqrt{2}}{\lambda \imath} \frac{\left(-j + e^{2e^{\frac{j\pi}{4}}u} - e^{2e^{\frac{3j\pi}{4}}u} + je^{2j\sqrt{2}u}\right)}{\left(1 + e^{2e^{\frac{j\pi}{4}}u} + e^{2e^{\frac{3j\pi}{4}}u} - 4e^{j\sqrt{2}u} + e^{2j\sqrt{2}u}\right)} & \frac{1}{\lambda^2 \imath} \frac{\left(-1 + e^{2e^{\frac{j\pi}{4}}u}\right)\left(-1 + e^{2e^{\frac{3j\pi}{4}}u}\right)}{\left(1 + e^{2e^{\frac{j\pi}{4}}u} + e^{2e^{\frac{3j\pi}{4}}u} - 4e^{j\sqrt{2}u} + e^{2j\sqrt{2}u}\right)} \\ \frac{1}{\lambda^2 \imath} \frac{\left(-1 + e^{2e^{\frac{j\pi}{4}}u}\right)\left(-1 + e^{2e^{\frac{3j\pi}{4}}u}\right)}{\left(1 + e^{2e^{\frac{j\pi}{4}}u} + e^{2e^{\frac{3j\pi}{4}}u} - 4e^{j\sqrt{2}u} + e^{2j\sqrt{2}u}\right)} & \frac{\sqrt{2}}{\lambda^3 \imath} \frac{\left(j + e^{2e^{\frac{j\pi}{4}}u} - e^{2e^{\frac{3j\pi}{4}}u} - je^{2j\sqrt{2}u}\right)}{\left(1 + e^{2e^{\frac{j\pi}{4}}u} + e^{2e^{\frac{3j\pi}{4}}u} - 4e^{j\sqrt{2}u} + e^{2j\sqrt{2}u}\right)} \end{pmatrix}. \tag{37}$$

Even though it is not explicit from eq. (37), V is found to be a real matrix, which is decent for a covariance matrix. The convergence is driven by a term proportional to $e^{-2ue^{\frac{j\pi}{4}}}$, which implies a convergence in $e^{-l\sqrt{2}/\lambda}$.

2.2.2. Variation of the angle variance along the track

We have considered above the optimal measurement of the track parameters at the vertex, $z = 0$. Here we examine the measurement at any position along the track. A track now consists of two segments (left and right), the fit of each of which provides an estimate with its own covariance matrix.

A first combination attempt is performed on the two variables (a and b) separately. As is obvious, if the detector is thick on both sides, the two estimates (right, left) of a track parameter (say: the angle) have the same uncertainty on the plateau and their optimal combination provides a gain in RMS precision of a factor of $\sqrt{2}$. But that neglected the fact that in the combination, the other variable should be constrained to have the same value on both sides too. With a weighted variance estimation, a further gain of a factor of $\sqrt{2}$ is obtained

on the plateau, that is a total gain of a factor of 2 with respect to individual measurements (Fig. 6) as was observed experimentally by running a KF on simulated tracks (Fig. 18 of [12]).

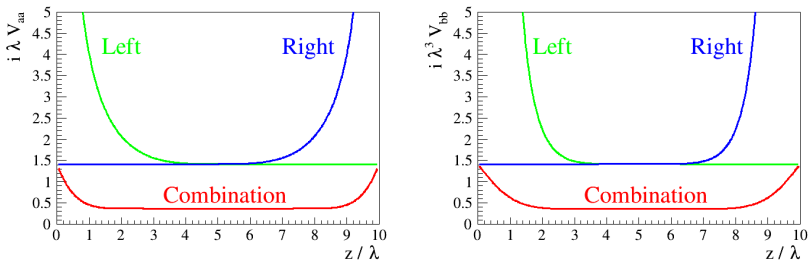

Figure 6: Normalized variance along the track for an $u = 10$ detector, as estimated from the left and from the right side, (eq. (37)) and of their optimal combination. Left plot: intercept. Right plot: angle. An improvement of a factor of 4 is visible on the plateau (i.e., far from the track ends), that corresponds to a factor of 2 for the standard deviation.

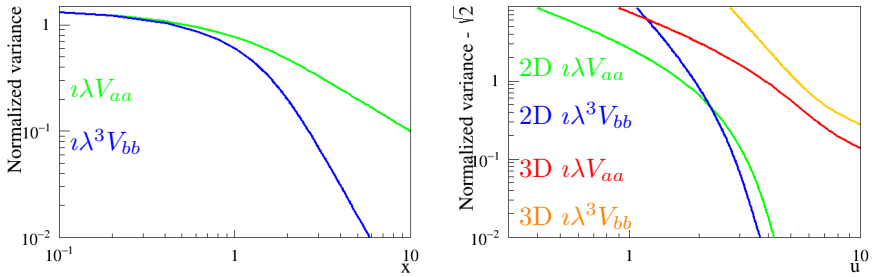

Figure 7: Exact solution wrap up: Thick detector (left) and homogeneous detector (right), for 2D ($B = 0$, no curvature) and 3D ($B \neq 0$, curvature) configurations. Normalized variance ($\imath\lambda V_{aa}$, and $\imath\lambda^3 V_{bb}$) minus the asymptote (either zero or $\sqrt{2}$), as a function of x and of u, respectively. Note that for the thick detector (left plots), the 2D and 3D expressions are found to be the same. Curves are from eq. (20) 2D thick detector and eq. (37) 2D homogeneous detector; the expressions in the 3D case are not shown in this paper.

2.3. Optimal tracking: wrap up

We now build on the results of the previous subsections to obtain expressions of the variances in terms of the detector parameters. We do so for segmented

detectors. The expressions for continuous detectors can be obtained with $\Delta x = l$.

$\imath \equiv$	$\frac{1}{l\sigma^2}$		information density per unit track length
$s \equiv$	$\left(\frac{p_0}{p}\right)^2 \frac{1}{X_0}\frac{\Delta x}{l}$		average multiple-scattering angle variance per unit track length
$\lambda \equiv \frac{1}{\sqrt[4]{\imath s}} \approx$	$\sqrt{l\sigma\sqrt{\frac{X_0}{\Delta x}}\frac{p}{p_0}}$		detector scattering length at momentum p
$x \equiv \frac{l}{\lambda} \approx$	$\sqrt{\frac{l}{\sigma}\frac{p_0}{p}\sqrt{\frac{\Delta x}{X_0}}}$		detector longitudinal sampling normalized to λ
$u \equiv \frac{L}{\lambda} \approx$	$N\sqrt{\frac{l}{\sigma}\frac{p_0}{p}\sqrt{\frac{\Delta x}{X_0}}}$		detector thickness normalized to λ

With:

- small x (large p), homogeneous detector (continuous equation),
- large x (small p), segmented detector (discrete equation)

and

- small u (large p), thin detector,
- large u (small p), thick detector.

The variances are found to be asymptotically:

		homogeneous $x < 0.2$	coarse $x > 2$
a	thin	$\frac{4}{\imath\lambda u} = \frac{4\sigma^2}{N}$ eq. (30)	
	thick	$\frac{\sqrt{2}}{\imath\lambda} = \sqrt{2}\left(\frac{p}{p_0}\right)^{-1/2}(l\sigma^3)^{1/2}\left(\frac{\Delta x}{X_0}\right)^{1/4}$ eq. (32)	$\frac{1}{\imath l} = \sigma^2$ eq. (23)
b	thin	$\frac{12}{\imath\lambda^3 u^3} = \frac{12\sigma^2}{l^2 N^3}$ eq. (31)	
	thick	$\frac{\sqrt{2}}{\imath\lambda^3} = \sqrt{2}\ \left(\frac{\sigma}{l}\right)^{1/2}\left(\frac{\Delta x}{X_0}\right)^{3/4}\left(\frac{p}{p_0}\right)^{-3/2} = \left(\frac{p}{p_1}\right)^{-3/2}$ eq. (32)	$\frac{2}{\imath l^3} = 2\left(\frac{\sigma}{l}\right)^2$ eq. (23)

where p_1 is a momentum that characterises the tracking angular-resolution properties of a detector affected by multiple scattering [12]

$$p_1 = p_0 \left(\frac{\Delta x}{X_0}\right)^{1/2} \left(\frac{2\sigma}{l}\right)^{1/3}. \tag{38}$$

- The two V_{aa} asymptotes cross for $u = u_{c,a} = 2\sqrt{2} \approx 2.83$;
- The two V_{bb} asymptotes cross for $u = u_{c,b} = (12/\sqrt{2})^{1/3} \approx 2.04$.

This, for a given detector, takes place for a value of the momentum p_u for which

$$u_c = N\sqrt{\frac{l}{\sigma}\frac{p_0}{p}\sqrt{\frac{\Delta x}{X_0}}}, \tag{39}$$

that is,

$$p_u = p_0\sqrt{\frac{\Delta x}{X_0}}\frac{N^2 l}{\sigma u_c^2}, \tag{40}$$

from which

$$u = u_c\sqrt{\frac{p_c}{p}}, \quad p = p_u\left(\frac{u_c}{u}\right)^2. \tag{41}$$

In short, a homogeneous detector is a thick detector, $u > u_c$, at low momentum, $p < p_u$ and a thin detector at higher momentum. In Table 1, we use $u_c = 2.5$ to compute the value of p_u.

Table 1: Parameters of two trackers considered in the text.

	gas argon TPC	liquid argon TPC	silicon detector		
X_0	2351.	14.0	9.4	cm	
l	0.1	0.3	1.0	cm	
Δx	l	l	0.0500	cm	
σ	0.1	0.1	0.0070	cm	
L	30.	1000.		cm	
N	300	3 333	56		
p_1	0.112	1.739	0.239	MeV/c	eq. (38)
p_u	1277.	10 614 042.	71 098.	MeV/c	eq. (40)
p_x	2.2	149.	3 542.	MeV/c	eq. (42)
p_s	0.024	5.4	16.6	MeV/c	eq. (61)
p_ℓ	352.	2 931 742.	19 638.	MeV/c	eq. (62)

In the same way, a detector is a homogeneous detector, $x < x_c$ at high momentum, $p > p_x$, with

$$p_x = p_0 \sqrt{\frac{\Delta x}{X_0}} \frac{l}{\sigma x_c^2}. \tag{42}$$

and $x_c = 0.2$ (Fig. 4). And similarly:

$$x = x_c \sqrt{\frac{p_c}{p}}, \quad p = p_x \left(\frac{x_c}{x}\right)^2. \tag{43}$$

- **Argon gas TPC**. We see that $p_u > p > p_x$ for most of the [1 MeV - 1 GeV] momentum range that is the primary target of the high-performance γ-ray telescopes mentioned above: the telescope is both a homogeneous and a thick detector.

- **Silicon detector**. Here the telescope is a segmented and a thick detector for most of the momentum range.

Note that the equality $p_u = p_x$ holds for $N = u_c/x_c$, that is, $N = 2.5/0.2 = 12.5$, so for most conceivable detectors, $p_u > p_x$, that is,

- if $p > p_u$ then $p > p_x$, if a detector is thin for a given track, then it's also homogeneous;
- if $p < p_x$ then $p < p_u$, if a detector is segmented for a given track, then it's also thick.

3. Kalman filter

A Kalman filter is an estimator of the state of a linear dynamic system perturbed by Gaussian white noise using measurements that are linear functions of the system state and corrupted by additive Gaussian white noise [29]. The paraxial propagation of a high-momentum particle inside a detector is affected by angular deflections due to scattering on the charged particles (electrons, nuclei) present in the detector matter. Deflections undergone at different locations on the track are uncorrelated, "white process noise", and are approximated to have a Gaussian distribution under the multiple-scattering approximation. Transverse position measurements are performed at several locations along the track. They are affected by an uncertainty that does not correlate from layer to layer, "white measurement noise", and that most often can be approximated by a Gaussian distribution. Angular deflections and measurement uncertainty are not correlated. When the system is non-linear, such as for the propagation in a magnetic field, it is linearized locally, "extended Kalman filter" ([33] and references therein). In the case of most particle detectors, the geometric, the multiple scattering and the measurement properties of the detector are uniform (at least piecewise) so the dynamics of the particle is described by a time-invariant system.

Since the founding work by Frühwirth [23], KF tracking has been used largely in high-energy physics. We present here a short description of the elements that are used in the next section, in a Bayesian formulation. Denoting $\{z_n^0\}$ and $\{z_n^m\}$ the true and the measured positions of a particle at layer n, respectively, and x_n the corresponding state vector, $\hat{x}_n = \mathbb{E}(x_n|z_0^m, \cdots, z_n^m)$ is the estimator of x_n conditioned to $\{z_0^m, \cdots, z_n^m\}$ and $x_n^{n-1} = \mathbb{E}(x_n|z_0^m, \cdots, z_{n-1}^m)$ is the prediction

of x_n given $\{z_0^m, \cdots, z_{n-1}^m\}$. x_n is obtained from x_{n-1}

$$x_n = D \cdot x_{n-1} + D \cdot \begin{bmatrix} 0 \\ u_n \end{bmatrix}; \tag{44}$$

u_n is the Gaussian-distributed deflection angle with variance sl. The covariance matrix of the state vectors is $P_n = \mathbb{E}((\hat{x}_n - x_n)(\hat{x}_n - x_n)^T | z_0, \cdots, z_n^m)$. The optimal estimator of x_n is obtained from $\hat{x}_{n-1}$ and from the measurements $\{z_0^m, \cdots, z_{n-1}^m\}$,

$$x_n^{n-1} = D\hat{x}_{n-1}, \tag{45}$$

$$P_n^{n-1} = D(P_{n-1} + B)D^T, \tag{46}$$

with

$$z_m^n = Hx_n + v_n, \tag{47}$$

where $H = \begin{bmatrix} 0 & 1 \end{bmatrix}$ is the measurement matrix and v_n is the measurement uncertainty which is Gaussian-distributed with variance $\sigma^2 = \dfrac{1}{il}$. The innovations are the difference between measurement and prediction,

$$\nu_n = z_n^m - x_n^{n-1} \tag{48}$$

and their variance is

$$S_n = \mathrm{Cov}(\nu_n) = \sigma^2 + HP_n^{n-1}H^T. \tag{49}$$

The gain matrix of the filter is

$$K_n = P_n^{n-1}H^T S_n^{-1}. \tag{50}$$

For the optimal value of the gain that minimizes the variance of the innovations, we obtain [29]

$$\hat{x}_n = x_n^{n-1} + K_n\nu_n, \tag{51}$$

$$P_n = P_n^{n-1} - K_n S_n K_n^T. \tag{52}$$

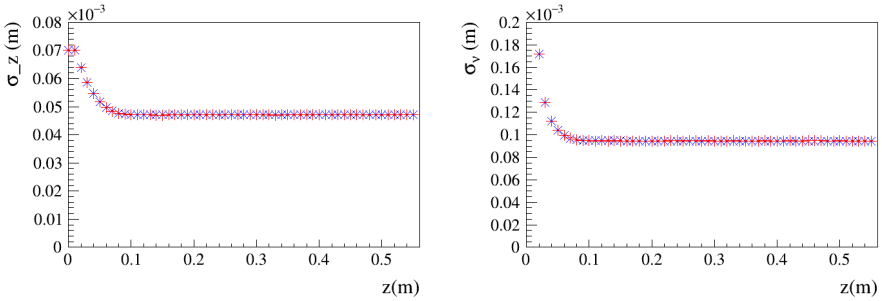

Figure 8: Kalman filter validation: RMS (plusses) of the position residues (left) and of the innovation residues (right) as a function of the longitudinal position in the tracker, for a sample of 10^6 50 MeV/c tracks in a silicon detector, compared to the RMS (crosses) computed from their variances, P_n and S_n, respectively.

Noting $Z^n = z_0^m, \cdots, z_n^m$ the set of measurements up to layer n and p the probability density,

$$\begin{aligned} p(Z^n) &= p(z_n^m, Z^{n-1}) \\ &= p(z_n^m|Z^{n-1})p(Z^{n-1}) \qquad \text{(Bayes)} \\ &= \prod_{i=0}^{n} p(z_i^m|Z^{i-1}) \qquad \text{(recurrence)}. \end{aligned} \tag{53}$$

As $z_i^m|Z^{i-1}$ is Gaussian distributed $\mathcal{N}(z_i, S_i)$:

$$p(z_i^m|Z^{i-1}) = \frac{1}{\sqrt{2\pi S_i}} \exp\left[-\frac{\nu_i^2}{2S_i}\right]. \tag{54}$$

We have implemented such a KF tracking software. Figure 8 shows a couple of sanity-check validation plots, the RMS of the position residues (left) and of the innovation residues (right) as a function of the longitudinal position in the tracker, for a sample of 10^6 50 MeV/c tracks in a silicon detector, compared to the RMS computed from their variance, P_n and S_n, respectively.

4. Momentum Measurement

A Kalman filter is the optimal linear estimator of the state vector of a dynamical system at the condition that the model be an accurate description of

the dynamics of the system and that the process and measurement noise covariance matrices be known, that is here, that the track momentum be known. The estimation of the noise covariance matrices of a dynamic system was pioneered by Mehra [34, 35] who studied and compared several methods:

- A Bayesian method that is the root of that we use in this work.
- Maximum likelihood methods, if necessary of both the state vector of the system and the noise matrices at the same time.

Bayesian and maximum likelihood methods were deemed to be too CPU consuming for the time.

- Covariance-matching techniques, making the innovation residuals consistent with their theoretical covariances; these methods were shown later to give biased estimates of the covariance matrices.
- Correlation methods, in particular based on the observation that when the KF gain K is optimal, the innovations of the filtering process are white and Gaussian.

Mehra showed that the optimal gain K can be determined uniquely, after which many efforts and publications have then been spent in determining the convergence of these methods and to which values of the process and measurement noise matrices they were, eventually, converging. In 2006, Odelson *et al.* [36] re-examined Mehra's work, showed that the definite positiveness of the matrices was not assured; based on the fact that the autocorrelation of the innovation sequence is linearly dependent on the noise covariances [37], they developed an autocovariance least-square (ALS) method that provides unbiased estimates of the noise matrices and that includes a mechanism that enforces definite positiveness [36].

Kalman filters have already been used for momentum measurement in non-magnetic particle physics detectors in the past ([38, 39]. The trick is to augment the state vector with the parameter vector to $(x, y, \mathrm{d}x/\mathrm{d}z, \mathrm{d}y/\mathrm{d}z, 1/p)$ so that

the KF performs their estimation simultaneously. However, this augmentation approach has been originally intended for estimating parameters in deterministic part of the model and its straightforward application for noise covariance matrices does not result in appropriate estimates ([40] and references therein).

In the case of charged particle tracking in a magnetic-field-free detector, the augmentation method was found to provide unbiased results though [38, 39], most likely as the tracking part and the deflection part of the filter behave as two separate filters, "only" linked by the joint uses of the track momentum, one for the process noise matrix, the other as part of the state vector. Also it enables the optimal treatment of energy loss and therefore it provides an improvement of about a factor of two with respect to the Molière method [39]. If would be interesting to examine to what extent they are efficient or even whether they are optimal. Note that in that scheme, the track has to be segmented to measure the track angle on each segment (in $\approx 19\,\mathrm{cm}$ long segments that contain ≈ 57 hits on average for[39], from which they obtain a relative resolution of 16 % on a sample of 4 m tracks with momenta ranging from 0.5 to $4.5\,\mathrm{GeV}/c$). (See also [41]).

4.1. Single track momentum measurement: Bayesian method

Following Matisko and Havlena [24] we obtain [3], from the measurements, the most probable value of s, and we extract from it an optimal estimator $\hat{p}$ of p. For an event A, defining $p_n(A) \equiv p(A|Z^n)$, we have

$$\begin{aligned} p_n(s) &= \frac{p_{n-1}(s, z_n^m)}{p_{n-1}(z_n^m)} \\ &= \frac{p_{n-1}(s) p_{n-1}(z_n^m|s)}{p_{n-1}(z_n^m)}. \end{aligned} \tag{55}$$

We name s-filter a KF with a gain matrix computed with a given value of s. We remember (eq. (49)) that the s-filter innovation probability density function (pdf) $\beta_n = p_{n-1}(z_n^m|s)$, is a normal, $\beta_n = \mathcal{N}(\nu_n(s), 0, S_n(s))$, where $\nu_n(s)$ and

[3] We assume that the detector spatial resolution σ is known either from calibration on beam or from the analysis of high momentum tracks.

$S_n(s)$ are computed during the filtering process. The $1/p_{n-1}(z_n^m)$ factor does not vary with s and is therefore neglected. We obtain

$$p_n(s) \propto \prod_i \beta_i. \tag{56}$$

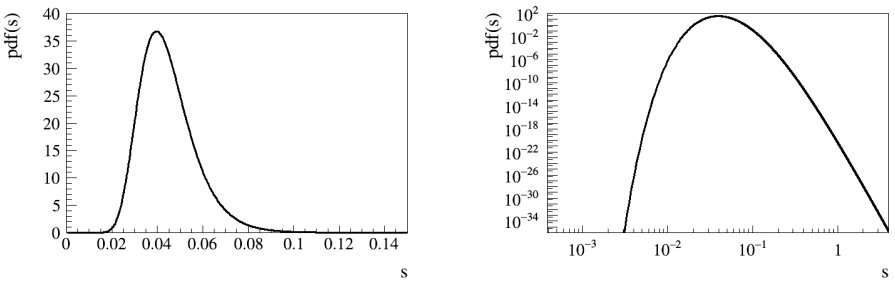

Figure 9: $p(s)$ distribution for a 50 MeV/c track in a silicon detector (eq. (56)). On that track, the momentum is measured to be equal to 49.9 MeV/c. Linear (left) and logarithmic (right) scales.

The distribution of $p(s)$ for one simulated 50 MeV/c track is shown in Fig. 9. The track momentum is then obtained from the value of s that maximizes $p_n(s)$:

$$p = p_0 \sqrt{\frac{\Delta x}{l X_0 s}}. \tag{57}$$

From the full width half maximum (FWHM) of $p(s)$ we calculate RMS_s/s and $\mathrm{RMS}_p/p = (\mathrm{RMS}_s/s)/2$. The average value of RMS_p/p is found to be much smaller than the relative RMS σ_p/p of the momentum measurements performed on a sample of tracks and shown in Figs. 10 and 11. Our interpretation is that the range of s values compatible within uncertainties with the deflection sample of a given track and the fluctuation of the deflection sample from track to track are separate quantities. In addition, we observe that the single-track $p(s)$ width and the measured momentum for that track are weakly correlated, so the former would add little information to the measurement of the latter.

We were not able to obtain an analytical expression for the relative precision of the momentum measurement. Instead we performed a parametric variation study for a silicon detector with

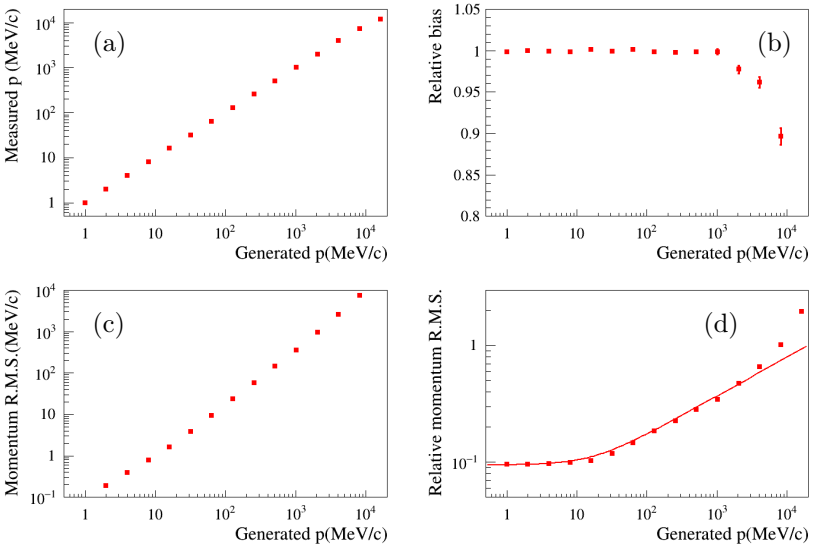

Figure 10: Performance of the momentum measurement for the silicon detector: Variation as a function of the true (generated) particle momentum of (a) the average measured momentum; (b) the average measured normalized to the generated momentum; (c) R.M.S of the measured momenta; (d) the relative R.M.S of the measured momenta. The curve is from eq. (58).

- $l = 0.5, 1.0, 2.0\,\mathrm{cm}$,
- $X_0 = 4.685, 9.37, 18.74\,\mathrm{cm}$,
- $N = 23, 46, 56, 92$,
- $\sigma^2 = 2.5, 5.0, 10.0 \times 10^{-5}\,\mathrm{cm}^2$,
- $p = 1 \cdots 2048\,\mathrm{MeV}/c$

and with $\Delta x = 500\,\mu\mathrm{m}$. A good representation of these data is obtained with the following expression:

$$\frac{\sigma_p}{p} \approx \frac{1}{\sqrt{2N}} \sqrt[4]{1 + 256 \left(\frac{p}{p_0}\right)^{4/3} \left(\frac{\sigma^2 X_0}{N \Delta x\ l^2}\right)^{2/3}}, \tag{58}$$

- from which we obtain the obvious low-momentum asymptote

$$\frac{\sigma_p}{p} \approx \frac{1}{\sqrt{2N}} \tag{59}$$

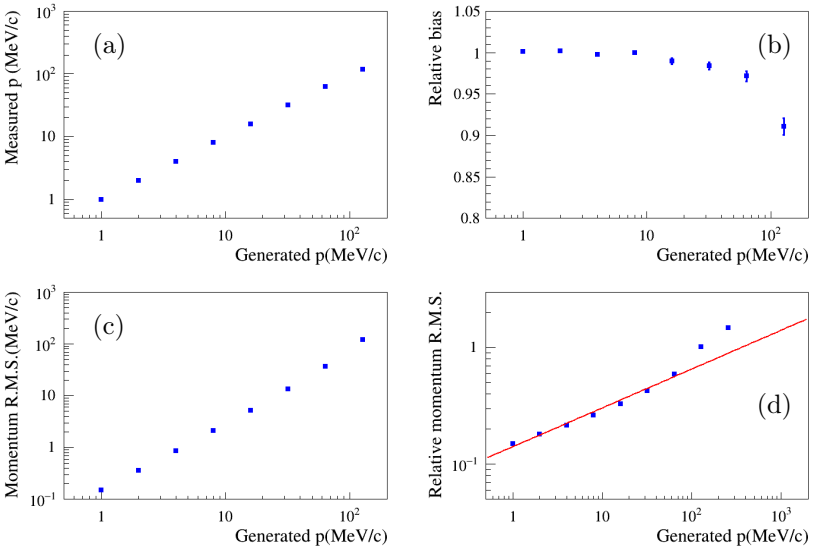

Figure 11: Performance of the momentum measurement for the argon gas detector: Variation as a function of the true (generated) particle momentum of (a) the average measured momentum; (b) the average measured normalized to the generated momentum; (c) R.M.S of the measured momenta; (d) the relative R.M.S of the measured momenta. The curve is from eq. (58).

- and the high-momentum asymptote

$$\frac{\sigma_p}{p} \approx \sqrt{\frac{8}{N}} \left(\frac{p}{p_0}\right)^{1/3} \left(\frac{\sigma^2 X_0}{N\Delta x\ l^2}\right)^{1/6}. \tag{60}$$

Of particular interest is the momentum, p_s, above which σ_p/p starts to depart from the low momentum asymptote,

$$p_s = p_0 \frac{1}{64} \left(\frac{N\Delta x\ l^2}{\sigma^2 X_0}\right)^{1/2}. \tag{61}$$

We define also the momentum, p_l, above which σ_p/p is larger than unity, which means that the measurement becomes meaningless:

$$p_\ell = p_0 \left(\frac{N}{8}\right)^{3/2} \left(\frac{N\Delta x\ l^2}{\sigma^2 X_0}\right)^{1/2}. \tag{62}$$

The only thing that can be said then is that that track is a straight track within uncertainties, that is, with inverse momentum $1/p$ compatible with zero. These

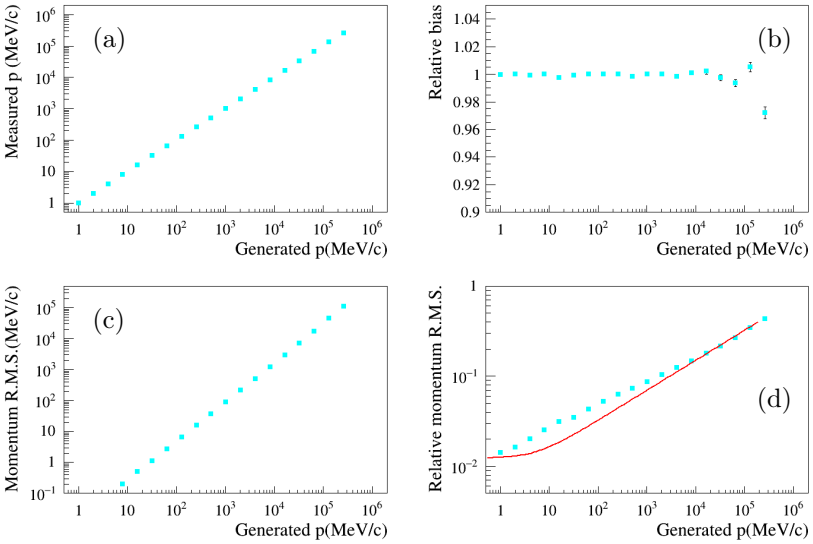

Figure 12: Performance of the momentum measurement for the liquid argon detector: Variation as a function of the true (generated) particle momentum of (a) the average measured momentum; (b) the average measured normalized to the generated momentum; (c) R.M.S of the measured momenta; (d) the relative R.M.S of the measured momenta. The curve is from eq. (58). The discrepancy between the data and the curve for this large-n detector, at low momentum that is at very low σ_p/p, needs further investigation.

two momenta are characteristics of the ability to measure track momenta with a given detector and are related to each other,

$$p_\ell = p_s \, (2N)^{3/2} \, . \tag{63}$$

Finally, we obtain a simpler expression of the relative momentum resolution,

$$\frac{\sigma_p}{p} \approx \frac{1}{\sqrt{2N}} \sqrt[4]{1 + \left(\frac{p}{p_s}\right)^{4/3}} \tag{64}$$

The target relative precision of the DUNE project of 18 % is within reach for 10 m tracks up to a momentum of 17.1 GeV/c with detector parameter values from Table 1 (Fig. 12).

4.2. Comparison with the cell-optimization result

For the continuous detector, $\Delta x = l$, eq. (60) becomes

$$\frac{\sigma_p}{p} = \frac{4}{N^{1/6}\sqrt{2L}} \left(\frac{p}{p_0}\right)^{1/3} \left(\sigma^2 X_0\right)^{1/6}, \tag{65}$$

that we can compare to the cell-optimization expression (eq. (12) of [11]):

$$\frac{\sigma_p}{p} = \frac{C}{\sqrt{2L}} \left(\frac{p}{p_0}\right)^{1/3} \left(\sigma^2 X_0\right)^{1/6} \tag{66}$$

with $C \equiv 5^{1/6} + 5^{-5/6} \approx 1.57$. We see that the precisions are commensurate at small N and that the present approach becomes more precise at larger N, within the high-momentum approximation, $p \gg p_s$.

4.3. Cramér-Rao Bounds

The Cramér-Rao bound is a lower bound on the variance of an estimator. If the variance of the estimator reaches the Cramér-Rao bound, it can be stated that the estimate is optimal. The Cramér-Rao criterion for an estimator $\hat{\theta}$ of a parameter θ obtained from measurements Z^N is [42]:

$$I(\theta) = -\mathbb{E}\left(\partial_\theta \left[\partial_\theta p(Z^N|\theta)\right]\right), \tag{67}$$

where I is the Fischer information. If $\hat{\theta}$ is an unbiased estimator of θ, then

$$\mathbb{E}\left((\hat{\theta} - \theta)^2\right) \geq I^{-1}(\theta). \tag{68}$$

Following the recursive method of [42] we obtain

$$I(s) = \frac{N}{2s^2}, \tag{69}$$

that is, finally, the obvious

$$\frac{\sigma_p}{p} \geq \frac{1}{\sqrt{2N}}. \tag{70}$$

No major insight obtained with the Cramér-Rao Bounds then.

4.4. Smoothing and Momentum Measurement

In this section 4 we have obtained an optimal estimator of a charged particle momentum based on the analysis of the filtering innovations of KFs with variable s parameters. After filtering, a KF provides an optimal estimate of the state vector parameters (transverse position and angle) of the track at the end of the track. An optimal estimate all along the track can be obtained by an additional, backward, pass named smoothing [23]. One might consider a scheme for momentum measurement based on the smoothing innovations rather than on the filtering innovations in the hope that the performance would be even better.

Actually smoothing is equivalent to an optimal linear combination of two independent filterings performed in the direct and in the backward directions, respectively [43]. We have compared the values of the estimators of the particle momentum obtained in the two directions and found them to be equal for each track. Therefore no further improvement is to be expected with such a combination, nor with a measurement based on smoothing innovations.

5. Conclusion

We first reconsider tracking with multiple scattering and detector resolution in magnetic-field-free detectors under the assumption that the track momentum is known, using optimal methods. This is done under a number of approximations, including Gaussian-distributed multiple-scattering deflections and the absence of energy loss during propagation. The information matrix is updated recursively while the track proceeds through the detector: after this mechanism has converged, the information matrix is found to be a solution of a Riccati equation which is not surprising as this optimal estimation can be performed with a Kalman filter.

For segmented detectors (discrete Riccati equation) and homogeneous detectors (continuous Riccati equation), we obtain exact expressions of the variances of the intercept and of the angle from the solution of that equation (eqs. (20)

and (37), respectively). We compare their Taylor expansions with expressions published in the past. Convergence (**thick detector**) takes place after a detector thickness $L \gtrsim 2.5\lambda$ for homogeneous detectors ($l \lesssim 0.2\lambda$), and for somewhat larger values of L for segmented detectors (Fig. 1). λ is the detector scattering length for track momentum p.

For a given track momentum, a **homogeneous detector** is defined as the small longitudinal sampling limit, $l \to 0$, $\imath$ and s being kept constant. In practice a limit of $l/\lambda \lesssim 0.2$ is found (Fig. 4). In contrast with magnetic spectrometers, for which the large L/λ Taylor expansion contains $1/(L/\lambda)^n$ terms, here ($\vec{B} = \vec{0}$), the expansion contains only exponential terms and convergence is therefore much faster (Fig. 7). For coarse segmented detectors for which $l/\lambda \gtrsim 2$, e.g. for $p \lesssim 35\,\mathrm{MeV}/c$ for eASTROGAM [8] or AMEGO [7] a KF becomes useless as the angular resolution is determined mainly by the measurements in the two first wafers (Fig. 3).

We then obtain an optimal estimator of the track momentum by a Bayesian analysis of the filtering innovations of a series of Kalman filters applied to the track. A numerical characterisation of the method shows that for a given detector the method is reliable up to some limit momentum p_ℓ above which the relative precision σ_p/p becomes larger than unity. For lower momentum tracks, $p \ll p_\ell$, the momentum estimation is found to be unbiased. We perform a parametric study of the estimator from which we extract a heuristic analytical description of the relative uncertainty of the momentum measurement (eq. (58)).

6. Acknowledgment

It is a pleasure to acknowledge the support of the French National Research Agency (ANR-13-BS05-0002).

α	one eigenvalue of Φ with norm larger than 1	eqs. (15), (16)
a	charged particle "intercept" at vertex	eq. (2)
b	charged particle slope at vertex	eq. (2)
A_n	matrix used in the calculation of I_n	Subsec. 2.1, see eq. (7)
B_n	matrix used in the calculation of I_n	Subsec. 2.1, see eq. (7)
B	scattering matrix	eq. (5)
B	magnetic field	Sec. 1
β	charged particle velocity normalized to the velocity of light in vacuum	Sec. 1, see eq. (1)
β	scale factor	Subsec. 2.1, see eq. (11)
β_n	Kalman innovation probability density	Subsec. 4.1, see eq. (56)
δ	neutrinos: CP-violating complex phase of the PMNS matrix	Sec. 1
D	drift matrix from layer n to layer $n+1$	eq. (4)
Δx	active target material thickness through which multiple scattering takes place	Sec. 1, see eq. (1)
E	photon energy	Sec. 1
$\mathbb{E}$	expectation value	Sec. 3
γ	charged particle Lorentz factor	Sec. 1
H	Kalman measurement matrix	Sec. 3, see eq. (47)
j	the imaginary unit	Subsec. 2.1
$\imath$	measurement information density per unit track length	Sec. 2, see eq. (6)
I	information matrix	eq. (3) and eq. (67)
J	a constant matrix	eq. (14
K	Kalman gain matrix	eq. (50)
L	total detector thickness	Sec. 2
l	space between two successive detector layers	Sec. 2, see eq. (4)
λ	detector scattering length at momentum p	eq. (17)
M	measurement matrix	eq. (6)
ν_n	Kalman innovations	eq. (48)
n	layer index	Sec. 2
N	number of layers in detector	Sec. 2
$\mathcal{N}$	normal or Gaussian probability density	eq. (54)
Φ	matrix that performs the transformation from $\begin{bmatrix} A_n \\ B_n \end{bmatrix}$ to $\begin{bmatrix} A_{n+1} \\ B_{n+1} \end{bmatrix}$	eq. (9)
p	probability density	Sec. 3, see eq. (53)
p	charged particle momentum	Sec. 1
p_0	multiple scattering constant	Sec. 1, see eq. (1)

p_1	detector tracking angle resolution characteristic momentum	eq. (38)
p_u	detector thin/thick limit momentum	eq. (40)
p_x	detector homogeneous/segmented limit momentum	eq. (42)
p_s	detector limit momentum between the $\sigma_p/p = 1/\sqrt{2N}$ and $\sigma_p/p \propto p^{1/3}$ ranges	eq. (61)
p_ℓ	detector limit momentum for which $\sigma_p/p = 1$	eq. (62)
P_n	Kalman state covariance matrix	Sec. 3, see eq. (46)
q	particle electric charge	Sec. 1
ρ	charged particle trajectory curvature radius	Sec. 1
σ	single-track single-layer space resolution	Sec. 1
σ_p	momentum resolution	Sec. 1
s	average multiple scattering angle variance per unit track length	Sec. 2, see eq. (5)
S_n	Kalman innovation covariance matrix	eq. (49)
θ	a parameter	Sec. 4.3, see eq. (67)
$\hat{\theta}$	estimator for parameter θ	Sec. 4.3, see eq. (67)
θ_0	multiple scattering RMS angle	eq. (1)
u	detector thickness normalized to detector scattering length at momentum p	eq. (18)
u_n	deflection angle	Sec. 3, see eq. (44)
v_n	Kalman measurement noise	Sec. 3, see eq. (47)
V	particle state vector ("intercept", angle) correlation matrix	Sec. 2, see eq. (3)
X_0	active target material radiation length	Sec. 1, see eq. (1)
x	detector longitudinal sampling normalized to scattering length at momentum p	Subsec. 2.1, see eq. (16)
x	axis name	
x_n	Kalman state vector	eq. (44)
X	matrix used in the calculation of Φ'	eq. (34)
Y	matrix used in the calculation of Φ'	eq. (34)
y	axis name	
z_n	Kalman measurements	eq. (47)
z	axis name	
Z	active target atomic number	Sec. 1
Z_n	set of measurements, $z_0 \cdots z_n$	Sec. 3, see eq. (53)

References

[1] T. Tanimori *et al.*, "Establishment of Imaging Spectroscopy of Nuclear Gamma-Rays based on Geometrical Optics," Sci. Rep. **7** (2017) 41511, [arXiv:1702.01483 [physics.ins-det]].

[2] T. J. O'Neill *et al.*, "The TIGRE gamma-ray telescope", AIP Conf. Proc. **587** (2001) 882.

[3] G. Kanbach *et al.*, "Development and calibration of the tracking Compton/Pair telescope MEGA", Nucl. Instrum. Meth. A **541** (2005) 310.

[4] F. Lebrun *et al.*, "CAPSiTT: Compton Large Area Silicon Timing Tracker for Cosmic Vision M3", PoS(**INTEGRAL 2010**) 034.

[5] A. Morselli *et al.*, "GAMMA-LIGHT: High-Energy Astrophysics above 10 MeV," Nuclear Physics B Proc. Supp. **239-240** (2013) 193.

[6] A. A. Moiseev *et al.*, "Compton-Pair Production Space Telescope (ComPair) for MeV Gamma-ray Astronomy," arXiv:1508.07349 [astro-ph.IM].

[7] J. McEnery *et al.*, "Allsky Medium Energy GammaRay Observatory (AMEGO)", Submitted to the Physics of the Cosmos Program Analysis Group Call for White Papers: Probe-Class Astrophysics Mission Concepts, March 2016.

[8] A. De Angelis, V. Tatischeff *et al.*, "The e-ASTROGAM mission: Exploring the extreme Universe with gamma rays in the MeV – GeV range", [arXiv:1611.02232], to appear in Exp Astron (2017), doi:10.1007/s10686-017-9533-6.

[9] X. Wu *et al.*, "PANGU: A High Resolution Gamma-ray Space Telescope," **SPIE2014** (2014) 91440F, [arXiv:1407.0710 [astro-ph.IM]].

[10] S. Takahashi *et al.*, "GRAINE project: The first balloon-borne, emulsion gamma-ray telescope experiment," PTEP **2015** (2015) 043H01.

[11] D. Bernard, "TPC in gamma-ray astronomy above pair-creation threshold," Nucl. Instrum. Meth. A **701**, 225 (2013) Erratum: [Nucl. Instrum. Meth. A **713**, 76 (2013)]. [arXiv:1211.1534 [astro-ph.IM]].

[12] D. Bernard, "Polarimetry of cosmic gamma-ray sources above e^+e^- pair creation threshold", Nucl. Instrum. Meth. A **729** (2013) 765. [arXiv:1307.3892 [astro-ph.IM]].

[13] P. Gros *et al.*, "Measurement of polarisation asymmetry for gamma rays between 1.7 to 74 MeV with the HARPO TPC", **SPIE2016**, 9905-95, arXiv:1606.09417 [astro-ph.IM].

[14] P. Gros and D. Bernard, "γ-ray polarimetry with conversions to e^+e^- pairs: polarization asymmetry and the way to measure it," Astropart. Phys. **88** (2017) 30, [arXiv:1611.05179 [astro-ph.IM]].

[15] D. Bernard, on behalf of the HARPO Collaboration, "HARPO: 1.7 - 74 MeV gamma-ray beam validation of a high angular resolution, high linear polarisation dilution, gas time projection chamber telescope and polarimeter," presented at SciNeGHE 2016, Pisa, Italy. Proceedings arXiv:1702.08429 [astro-ph.IM], to appear in Il Nuovo Cimento 40 C (2017).

[16] S. P. Wakely *et al.*, "Transition radiation detectors for energy measurements at high Lorentz factors," Nucl. Instrum. Meth. A **531** (2004) 435.

[17] R. Acciarri *et al.* [DUNE Collaboration], "Long-Baseline Neutrino Facility (LBNF) and Deep Underground Neutrino Experiment (DUNE) : Volume 2: The Physics Program for DUNE at LBNF," arXiv:1512.06148 [physics.ins-det].

[18] R. Acciarri *et al.* [DUNE Collaboration], "Long-Baseline Neutrino Facility (LBNF) and Deep Underground Neutrino Experiment (DUNE) : Volume 4 The DUNE Detectors at LBNF," arXiv:1601.02984 [physics.ins-det].

[19] A. Ankowski *et al.* [ICARUS Collaboration], "Measurement of through-going particle momentum by means of multiple scattering with the ICARUS T600 TPC," Eur. Phys. J. C **48** (2006) 667

[20] G. Molière, "Theorie der Streuung schneller geladener Teilchen. III. Die Vielfachstreuung von Bahnspuren unter Berüksichtigung der statistischen Kopplung", Zeitschrift Naturforschung A **10** (1955) 177.

[21] K. Kodama *et al.*, "Momentum measurement of secondary particle by multiple Coulomb scattering with emulsion cloud chamber in DONuT experiment," Nucl. Instrum. Meth. A **574** (2007) 192.

[22] N. Agafonova *et al.* [OPERA Collaboration], "Momentum measurement by the Multiple Coulomb Scattering method in the OPERA lead emulsion target," New J. Phys. **14** (2012) 013026 [arXiv:1106.6211 [physics.ins-det]].

[23] R. Frühwirth, "Application of Kalman filtering to track and vertex fitting," Nucl. Instrum. Meth. A **262** (1987) 444.

[24] P. Matisko and V. Havlena, "Noise covariance estimation for Kalman filter tuning using Bayesian approach and Monte Carlo", Int. J. Adapt. Control Signal Process. **27** (2013) 957.

[25] X. Wu, "PANGU: A High Resolution Gamma-Ray Space Telescope," PoS **ICRC2015** (2016) 964.

[26] C. Patrignani *et al.* [Particle Data Group], "Review of Particle Physics," Chin. Phys. C **40** (2016) 100001.

[27] P. Billoir, "Track Fitting With Multiple Scattering: A New Method," Nucl. Instrum. Meth. A **225** (1984) 352.

[28] W. R. Innes, "Some formulas for estimating tracking errors," Nucl. Instrum. Meth. A **329** (1993) 238.

[29] S. Grewal and P. Andrews, "Kalman Filtering, theory and practice using Matlab", 2nd edition, Wiley Interscience publication, (2001)

[30] M. Adam and N. Assimakis, "Nonrecursive solution for the discrete algebraic Riccati equation and $X + A * X - 1A = L$", Open Mathematics **13.1** (2015) 51-63.

[31] Wolfram Mathematica

[32] P. Yuantong "Hamiltonian Matrices and the Algebraic Riccati Equation", Technische Universität Chemnitz, 2009.

[33] K. Fujii, "Extended Kalman Filter" The ACFA-Sim-J Group

[34] R. K. Mehra, "On the identification of variances and adaptive Kalman filtering", IEEE Trans. Automat. Control **15** (1970) 175-184.

[35] Mehra, R., "Approaches to adaptive filtering", IEEE Trans. Automat. Control **17** (1972) 903-908.

[36] B. J. Odelson, M. R. Rajamani, J. B. Rawlings, "A new autocovariance least-squares method for estimating noise covariances", Automatica **42** (2006) 303-308.

[37] P. R. Belanger, "Estimation of noise covariance matrices for a linear time varying stochastic process", Automatica **10** (1974) 267-275.

[38] L. Stanco, "Particle track reconstruction in heavy materials with the Kalman technique," Comput. Phys. Commun. **57** (1989) 380.

[39] M. Antonello *et al.*, "Muon momentum measurement in ICARUS-T600 LAr-TPC via multiple scattering in few-GeV range," arXiv:1612.07715 [physics.ins-det].

[40] J. Duník, M. Ŝimandl, O. Straka, "Methods for Estimating State and Measurement Noise Covariance Matrices: Aspects and Comparison", IFAC Proceedings Volumes **42** (2009) 372-377.

[41] P. Abratenko *et al.* [MicroBooNE Collaboration], "Determination of muon momentum in the MicroBooNE LArTPC using an improved model of multiple Coulomb scattering," arXiv:1703.06187 [physics.ins-det].

[42] P. Matisko, V. Havlena, "Cramér-Rao Bounds for Estimation of Linear System Noise Covariances", Journal of Mechanical Engineering and Automation **2** (2012) 6-11.

[43] D. C. Fraser, "A New Technique for the Optimal Smoothing of Data", Sc.D. Dissertation, Mass. Inst. Tech., Cambridge, MA, 1967.

Contents